The Bioscan AN INTERNATIONAL QUARTERLY JOURNAL OF LIFE SCIENCES 20(4): 216-232, 2025 www.thebioscan.com

Molecular Docking-Guided Elucidation of Anti-inflammatory Potential of Vitex negundo: Targeting Prostaglandin E Synthase-2 and Cytokine Pathways

Jishamol K[1], Prajna P Shetty[2], Navami S[3], Gargi R Nair[4]
[1,2,3]Department of Biochemistry, Srinivas Institute of Medical Sciences & Research Center, Mangalore, India
[4]Department of Pathology, St. Gregorios college of health science, Pathanamthitta, India[4]

Corresponsding author: Jishamol K,
Email: jishapournami99@gmail.com

DOI: 10.63001/tbs.2025.v20.i04.pp216-232

KEYWORDS:
Vitex negundo, anti-inflammatory, cytokines, mPGES-2, molecular docking, natural therapeutics.

Received on:

01-09-2025

Accepted on:

04-10-2025

Published on:

08-11-2025

ABSTRACT

Background
Chronic inflammation plays a key role in various pathological conditions such as autoimmune diseases and cardiovascular disorders. Conventional anti-inflammatory drugs, though effective, pose risks with prolonged use. *Vitex negundo*, a medicinal plant widely used in traditional medicine, holds promise as a safer alternative due to its diverse phytochemical profile. However, its detailed cellular and molecular mechanisms remain underexplored.

Objectives
To evaluate the anti-inflammatory and cytoprotective potential of methanolic leaf extract of *Vitex negundo* using in-vitro assays and in-silico molecular docking, focusing on its modulation of pro-inflammatory cytokines and interactions with key inflammatory targets.

Methods
Molecular docking was performed for key bioactive compounds (e.g., casticin, kaempferol) against prostaglandin E synthase (mPGES-2, PDB: 1Z9H) a pivotal enzyme in prostaglandin biosynthesis using AutoDock Vina, and ADME profiling using SwissADME.

Results
Docking studies revealed Kaempferol and 6,7,4-Trimethoxyflavone as top binders (–7.15 kcal/mol) to mPGES-2, forming multiple stabilizing interactions with active site residues such as Ser166 and Asp239. ADME analysis showed that 7 out of 10 ligands complied with Lipinski's Rule of Five and had high gastrointestinal absorption, supporting their drug-likeness.

Conclusion
The Vitex negundo exhibits cytoprotective properties and effectively inhibits key pro-inflammatory cytokines. In-silico docking confirms its potential mechanism via direct interaction with mPGES-2. These findings validate its traditional use and support further development as a plant-derived anti-inflammatory therapeutic.

Introduction

Inflammation is a complex, tightly regulated response to tissue injury, infection, or harmful stimuli that is essential for healing. However, chronic or uncontrolled inflammation contributes to many pathological conditions, including autoimmune disorders, cardiovascular diseases, diabetes, and neurodegeneration (Ciesielski et al., 2022; Gusev & Zhuravleva, 2022). The inflammatory response is mediated by signaling molecules like cytokines and prostaglandins; key pro-inflammatory cytokines such as TNF-α, IL-6, IL-1β, and PGE2 drive inflammatory cascades. Conventional anti-inflammatory drugs (e.g., NSAIDs and corticosteroids) suppress these mediators, but long-term use can cause serious side effects such as gastrointestinal complications, immunosuppression, cardiovascular risks, and hormonal imbalances (Reichardt et al., 2021). Therefore, there is an urgent need for safer, sustainable anti-inflammatory alternatives from natural origins.

Plants have long been rich sources of bioactive compounds with medicinal properties. Among them, *Vitex negundo* L. (Verbenaceae), commonly known as "Nirgundi" or "chaste tree," is widely distributed in South and Southeast Asia and is renowned in traditional medicine for its analgesic, anti-inflammatory, and antioxidant effects (Praveen et al., 2020). Various parts of this plant (leaves, roots, seeds) are used in Ayurveda to treat pain, joint inflammation, skin diseases, and respiratory conditions. Phytochemical studies show that *Vitex negundo* contains a wide array of secondary metabolites (flavonoids, terpenoids, iridoids, lignans, essential oils), many of which exhibit anti-inflammatory activity (Dwivedi et al., 2021).

However, the full therapeutic potential of *Vitex negundo*, particularly its effects on key inflammatory mediators at the cellular and molecular levels, remains underexplored in modern pharmacology.

The present study aims to comprehensively evaluate the anti-inflammatory efficacy of *Vitex negundo* leaf extract through an integrative approach combining in-vitro cell-based assays and in-silico molecular modelling. Cytotoxicity was assessed by an MTT assay on L929 fibroblast cells to ensure the extract's safety at various concentrations. Enzyme-linked immunosorbent assays (ELISA) were used to quantify the extract's inhibition of major pro-inflammatory cytokines (TNF-α, IL-6, IL-1β, PGE2). Additionally, molecular docking was performed to assess the binding affinities of selected *Vitex negundo* phytoconstituents with key inflammatory targets such as Cyclooxygenase-2 (COX-2) and Penicillin-Binding Protein 3 (PBP3), and an ADME analysis evaluated the pharmacokinetic profiles and drug-likeness of these compounds. This integrative methodology will provide new insights into the pharmacological potential of *Vitex negundo*, highlighting its promise for developing natural, plant-based anti-inflammatory therapies.

Materials and Methods

Molecular docking was conducted to assess the interaction of selected phytoconstituents from *V. negundo* with the inflammatory target enzyme microsomal prostaglandin E synthase-2 (mPGES-2; PDB ID: 1Z9H). The protein structure was retrieved from the RCSB PDB, and co-crystallized ligands and water molecules were removed. Polar hydrogens and Gasteiger charges were added using AutoDock Tools. The docking grid (22 × 22 × 22 Å) was centered on the catalytic pocket containing Cys110, as determined using CASTp.

Ten ligands (see Supplementary Table S1) were selected based on phytochemical reports and retrieved from PubChem. Ligands were energy minimized and converted into PDBQT format. Docking was performed using AutoDock Vina (exhaustiveness = 8). The best binding pose for each ligand was analyzed using PyMOL and LigPlot+ to determine hydrogen bonding, hydrophobic interactions, and binding affinities.

ADME and Drug-Likeness Prediction

SwissADME was used to evaluate the pharmacokinetic properties of the docked phytoligands. SMILES strings were input to compute molecular descriptors including molecular weight, LogP, hydrogen bond donors/acceptors, gastrointestinal absorption, blood-brain barrier permeability, and bioavailability score. Lipinski's Rule of Five was applied to assess drug-likeness for each ligand.

Statistical Analysis

All assays were performed in triplicate and data were expressed as mean ± standard deviation (SD). Statistical analysis was conducted using one-way analysis of variance (ANOVA) followed by Dunnett's post hoc test. A p-value < 0.05 was considered statistically significant. Graphs and statistical outputs were generated using GraphPad Prism version 8.0.

Results

To elucidate the molecular mechanism underlying the anti-inflammatory activity of *Vitex negundo*, molecular docking studies were performed targeting prostaglandin E synthase-2 (mPGES-2), a terminal enzyme in the PGE_2 biosynthetic pathway. The 3D crystal structure of mPGES-2 (PDB ID: 1Z9H) complexed with indomethacin was retrieved from the Protein Data Bank. Protein preparation involved removal of water molecules, addition of polar hydrogens, and assignment of Gasteiger charges using AutoDock Tools 1.5.7.

Figure 1: Showing 3D structure of target protein (PDB: 1Z9H)

A panel of ten phytochemicals (*2,3-Dihydroxybenzoic acid, Artemetin, Casticin, Gardenin A, Geranyl acetate, Kaempferol, p-Hydroxybenzoic acid, Quinic acid, 6,7,4-Trimethoxyflavone, Caryophyllene oxide*)(See supplementary Table S1 for full compound details and) reported in *Vitex negundo* were selected for docking based on literature evidence of anti-inflammatory or bioactive properties. Ligand structures were obtained from the PubChem database in SDF format, energy-minimized using Open Babel, and converted to PDBQT using AutoDock Tools.

Active Site Prediction of Target Protein (PDB ID: 1Z9H)

To identify potential binding regions within the selected protein target (Cyclooxygenase, PDB ID: 1Z9H), CASTp analysis was employed. The tool identified significant cavities corresponding to plausible docking sites based on surface topology and pocket geometry.

The most prominent active site on Chain A was characterized by an "Area: 7825.577 Å²" and "Volume: 15,437.163 Å³".

Residue-level analysis revealed a cluster of amino acids within this binding pocket, indicating a structurally accessible and functionally relevant region for ligand interaction. The predicted active site residues are shown in Figure 2, with the active site highlighted in red within the 3D ribbon representation of the protein. Additionally, the amino acid sequence corresponding to Chain A is shown in Figure 13, where the active-site residues are highlighted in blue.

The active site of the target protein (PDB ID: 1Z9H, Chain A) was further analyzed to identify individual amino acids that form the binding cavity. Using CASTp analysis, a comprehensive list of interacting residues and their respective atomic coordinates was generated. This includes key residues such as TYR107, THR109, CYS110, PHE112, ARG137, LYS200, among others, which contribute to the structural and chemical environment of the binding site.

A complete list of amino acids and corresponding atoms involved in the

predicted active site pocket is provided in Supplementary Table S2.

Ligand Filtering and Drug-Likeness Assessment

All ten phytoconstituents were screened using SwissADME. Compounds satisfying Lipinski's Rule of Five and showing high gastrointestinal (GI) absorption with zero PAINS alerts were retained for docking (Table 4). Full SwissADME profiles, including TPSA, Log Kp, and synthetic accessibility scores, are provided in Supplementary Tables S3 to S13.

ADME Visualization and Drug-likeness

The pharmacokinetic and physicochemical profiles of all ten phytocompounds were visualized using SwissADME-generated bioavailability radar plots (Supplementary Table 1). These graphical summaries complemented the tabulated ADME data, confirming the overall suitability of selected ligands for oral drug-like behavior, with most compounds exhibiting favorable GI absorption and no major rule violations.

Molecular docking was performed using AutoDock Vina with default search parameters within a grid box encompassing the active site of mPGES-2. Each ligand was docked separately, and the top-ranked binding conformation was selected based on binding affinity (kcal/mol) and key molecular interactions.

All ten phytocompounds were docked with the active site of the target protein 1Z9H using AutoDock Vina. The results revealed distinct binding affinities, hydrogen bonding interactions, and hydrophobic contacts for each ligand. The binding affinity ranged from –4.41 to –7.15 kcal/mol. Notably, Lig6 (Kaempferol) and Lig9 (6,7,4-Trimethoxyflavone) exhibited the highest binding affinity (–7.15 kcal/mol). Lig6 formed six hydrogen bonds involving key residues such as Ser166, Asp239, and Tyr209, while Lig9, despite having only one hydrogen bond, engaged in extensive hydrophobic interactions with 14 amino acid residues. Of the 10 phytoligands docked, 7 fulfilled Lipinski's rule of five and showed high GI absorption, making them pharmacokinetically favorable candidates. A detailed summary of binding affinities, hydrogen bonding profiles, interacting residues, and interaction distances is presented in Table 5.

Ligand Code	Binding Affinity (kcal/mol)	No. of H-bonds	H-Bond Forming Amino Acids	H-Bond Distance (Å)	Hydrophobic Interaction Amino Acids	No. of Hydrophobic Interacting AAs
Lig1	-4.41	3	Asp164(A), Ser165(A), Val148(A)	2.78, 3.04, 2.48, 2.69, 3.07	Lys147(A), Phe112(A)	2
Lig2	-6.82	3	His244(A), Ser247(A), Thr109(A)	2.93, 3.10, 2.33, 2.96	Leu393(A), Phe112(A), Pro111(A), Cys110(A), Ile264(A), Val343(A), Tyr263(A), Ile246(A), Val243(A)	9
Lig3	-6.89	4	Ser247(A), Thr109(A), Lys108(A), Glu131(A)	3.14, 3.07, 3.34, 3.72, 2.67	Ile246(A), Val343(A), Val250(A), Ile264(A), Gly268(A), Val132(A), Pro134(A), Lys269(A),	10

					Tyr107(A), Phe270(A)	
Lig4	-6.62	3	His297(A), Tyr251(A), Thr109(A)	3.01, 3.18, 3.05	Phe112(A), His244(A), Pro248(A), Val243(A), Ile246(A), Pro111(A), Ser247(A), Val343(A), Ile264(A), Met286(A), Arg296(A), Leu293(A)	12
Lig5	-5.58	2	His244(A), Ser247(A)	2.92, 2.99	Pro111(A), Thr109(A), Val343(A), Ile264(A), Ile246(A), Ser260(A), Val250(A), Tyr251(A), Pro248(A), Val243(A)	10
Lig6	-7.15	6	Ser166(A), Asp239(A), Tyr209(A), Asp164(A), Ser165(A), Val148(A)	2.56, 2.55, 2.44, 2.83, 2.91, 2.99, 3.09	Lys115(A), Lys147(A), Phe112(A), Lys208(A)	4
Lig7	-4.81	3	Thr203(A), Lys147(A), Arg146(A)	2.78, 2.88, 2.69, 2.76	Val202(A), Tyr145(A)	2
Lig8	-4.88	5	Val148(A), Ser165(A), Asp164(A), Tyr145(A), Lys147(A)	2.91, 2.62, 2.83, 2.46, 2.92, 2.62, 3.12, 2.68	Phe112(A), Pro149(A)	2
Lig9	-7.15	1	Thr109(A)	3.13	Ile246(A), Val250(A), Val342(A), Ile264(A), Pro134(A), Phe270(A), Lys269(A), Gly263(A), Glu131(A), Val132(A), Tyr107(A), Cys110(A), Pro111(A), Ser247(A)	14
Lig10	-6.63	0	-	-	Phe270(A), Ile264(A), Cys110(A), Tyr107(A), Thr109(A), Glu131(A),	9

					Val132(A), Pro134(A), Gly268(A)	

Table 5. Affinity scores and molecular interactions of selected phytocompounds with the active site of Cyclooxygenase (PDB ID: 1Z9H). Values include binding affinities (kcal/mol), hydrogen bond counts, bond-forming amino acid residues and distances, and hydrophobic interactions.

Representative 2D and 3D molecular docking interaction profiles of each ligand with the target protein (PDB ID: 1Z9H) are illustrated below. These include hydrogen bonding, hydrophobic contacts, and orientation within the active pocket. LigPlot+ diagrams highlight polar interactions and hydrophobic residues, while 3D visualizations from UCSF Chimera provide spatial confirmation of binding conformations. Figures 4 to 13 correspond to each ligand and depict both the 2D interaction schematic and the 3D docking pose with active site residues. These visualizations support the numerical results from Table 14 and offer structural evidence for ligand efficacy and selectivity.

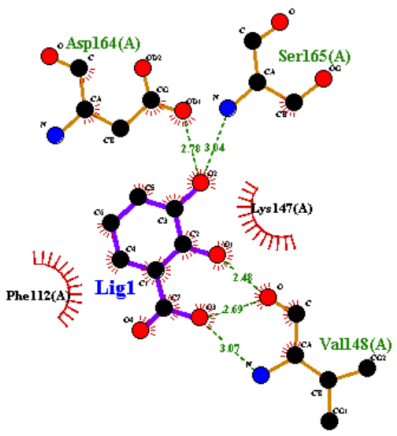

2,3-dihydroxybenzoic acid

Figure 4A: 2D LigPlot+ interaction diagram of Lig1 showing hydrogen bonding (green dashed lines), and hydrophobic contacts (red arcs) with mPGES-2.

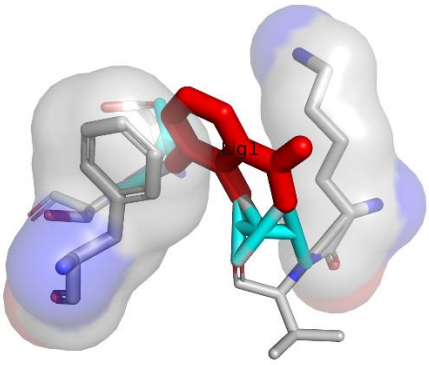

Figure 4B: 3D interaction model of Lig1 within the active site of mPGES-2, illustrating key hydrogen bonds and hydrophobic interactions. The ligand is shown in stick representation (cyan), while interacting residues are visualized with electrostatic surface rendering.

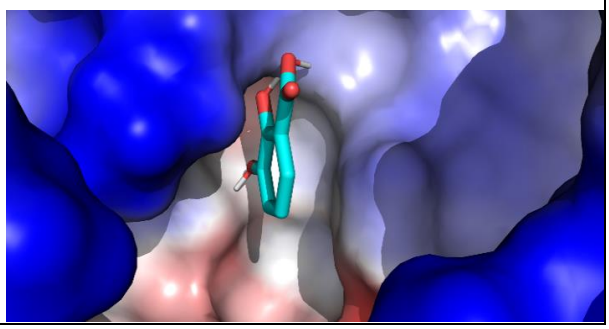

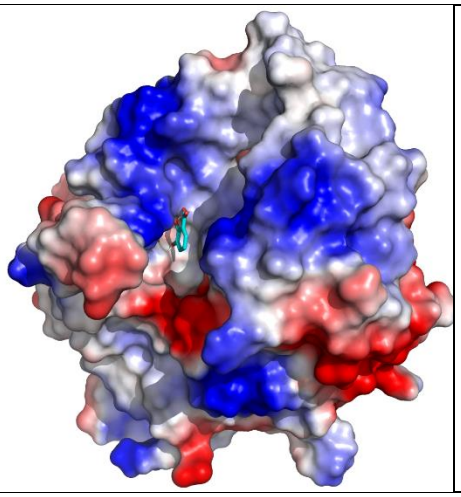

Figure 4C: 3D representation of mPGES-2 highlighting the electrostatic potential surface (blue: positive, red: negative) and the bound pose Lig1 (shown in cyan stick) embedded within the binding cavity.

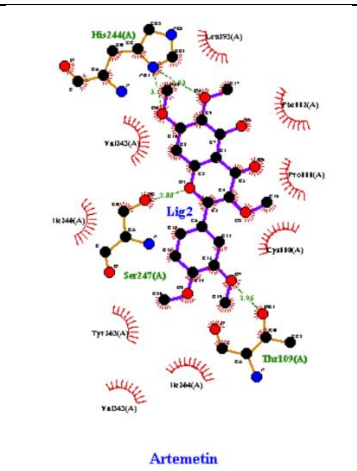

Figure 5A: 2D LigPlot+ interaction diagram of Lig2 showing hydrogen bonding (green dashed lines) and hydrophobic contacts (red arcs) with mPGES-2.

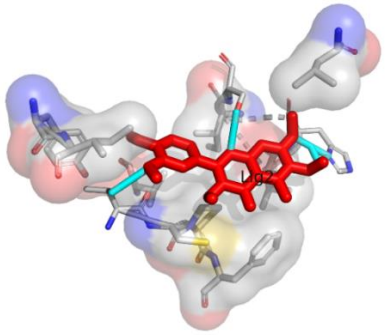

Figure 5B: 3D interaction model of Lig2 within the active site of mPGES-2, illustrating key hydrogen bonds and hydrophobic interactions. The ligand is shown in stick representation (cyan), while interacting residues are visualized with electrostatic surface rendering.

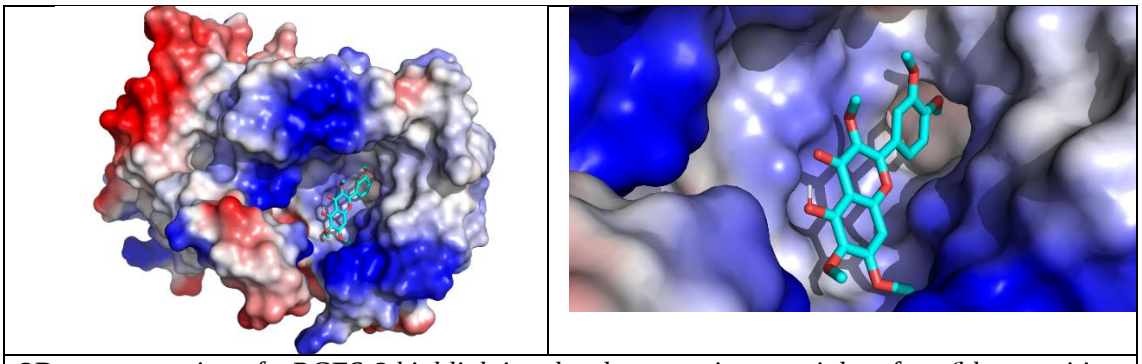

3D representation of mPGES-2 highlighting the electrostatic potential surface (blue: positive, red: negative) and the bound pose Lig2 (shown in cyan stick) embedded within the binding cavity.

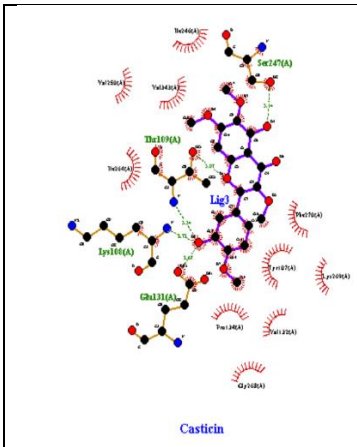

Figure 6A: 2D LigPlot+ interaction diagram of Lig3 showing hydrogen bonding (green dashed lines), and hydrophobic contacts (red arcs) with mPGES-2.

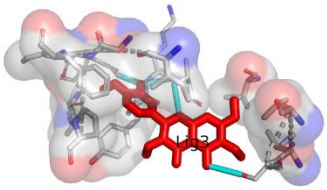

Figure 6B: 3D interaction model of Lig3 within the active site of mPGES-2, illustrating key hydrogen bonds and hydrophobic interactions. The ligand is shown in stick representation (cyan), while interacting residues are visualized with electrostatic surface rendering.

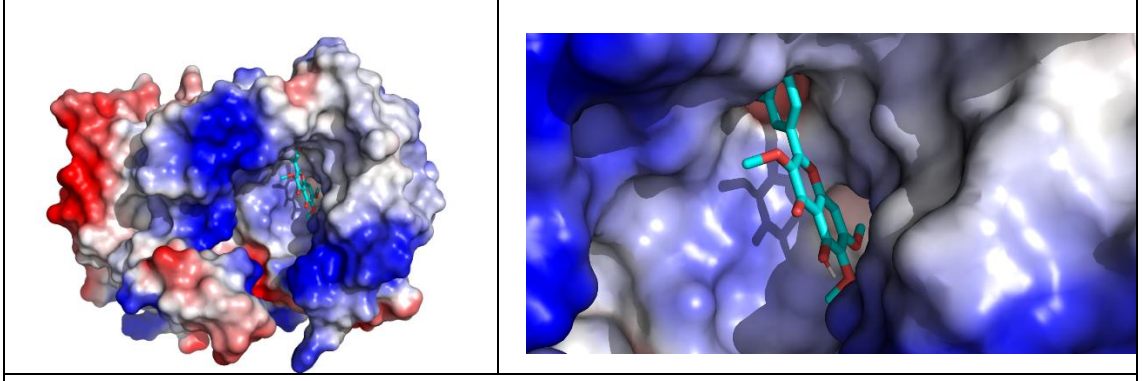

Figure 6C: 3D representation of mPGES-2 highlighting the electrostatic potential surface (blue: positive, red: negative) and the bound pose Lig3 (shown in cyan stick) embedded within the binding cavity.

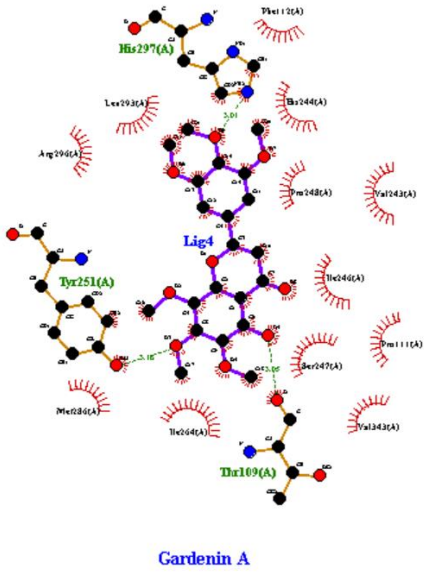

Figure 7A: 2D LigPlot+ interaction diagram of Lig4 showing hydrogen bonding (green dashed lines), and hydrophobic contacts (red arcs) with mPGES-2.

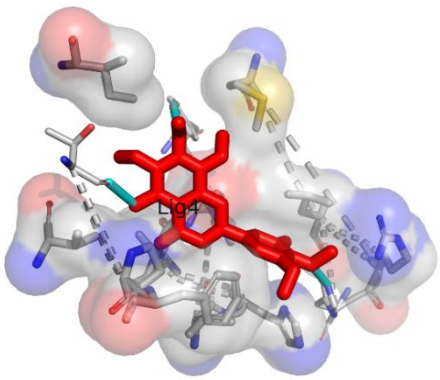

Figure 7B: 3D interaction model of Lig4 within the active site of mPGES-2, illustrating key hydrogen bonds and hydrophobic interactions. The ligand is shown in stick representation (cyan), while interacting residues are visualized with electrostatic surface rendering.

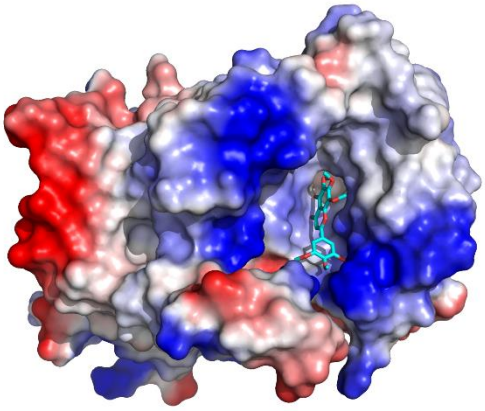

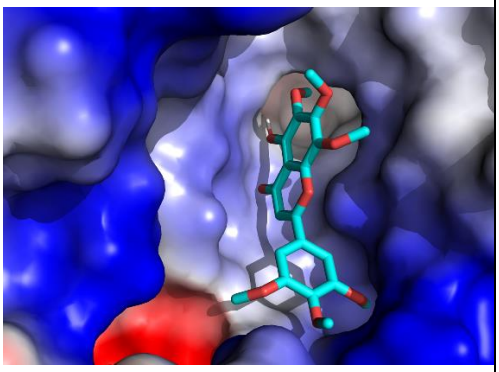

Figure 7C: 3D representation of mPGES-2 highlighting the electrostatic potential surface (blue: positive, red: negative) and the bound pose Lig4 (shown in cyan stick) embedded within the binding cavity.

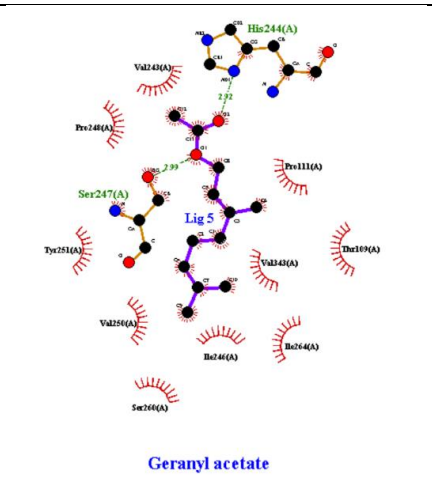

Figure 8A: 2D LigPlot+ interaction diagram of Lig5 showing hydrogen bonding (green dashed lines), and hydrophobic contacts (red arcs) with mPGES-2.

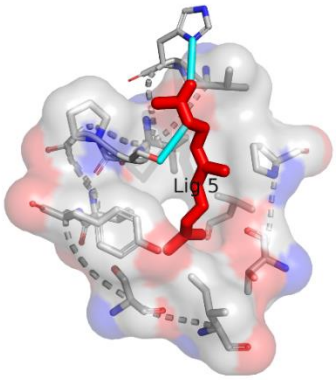

Figure 8B: 3D interaction model of Lig5 within the active site of mPGES-2, illustrating key hydrogen bonds and hydrophobic interactions. The ligand is shown in stick representation (cyan), while interacting residues are visualized with electrostatic surface rendering.

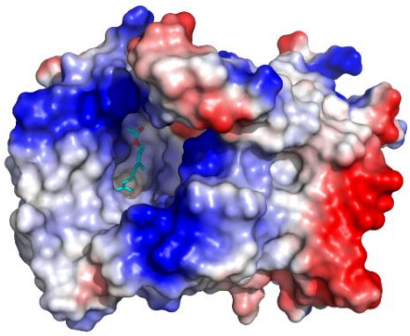

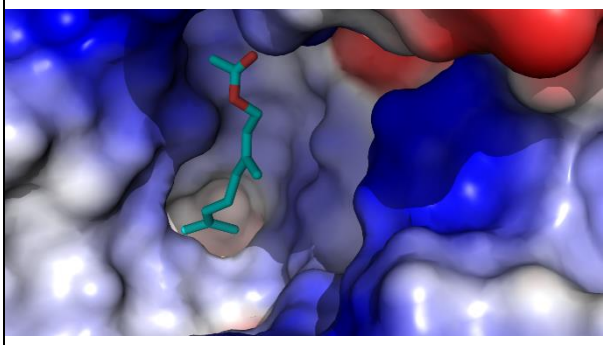

Figure 8C: 3D representation of mPGES-2 highlighting the electrostatic potential surface (blue: positive, red: negative) and the bound pose Lig5 (shown in cyan stick) embedded within the binding cavity.

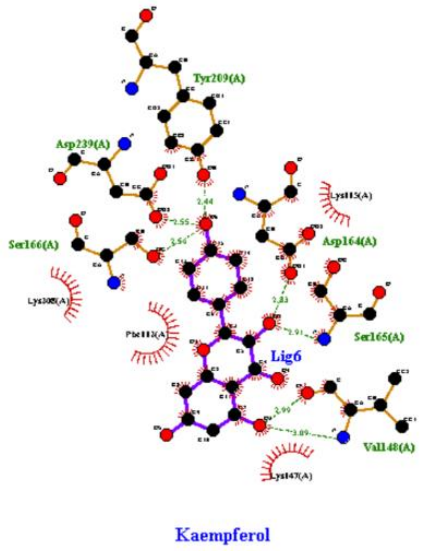

Figure 9A: 2D LigPlot+ interaction diagram of Lig6 showing hydrogen bonding (green dashed lines), and hydrophobic contacts (red arcs) with mPGES-2.

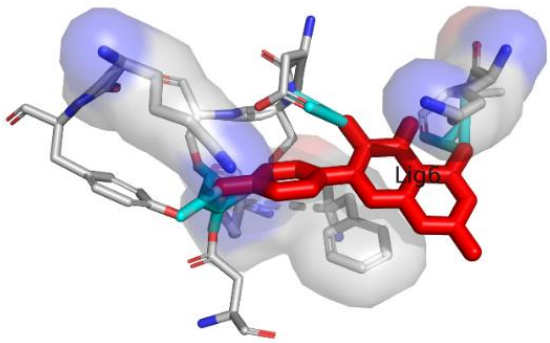

Figure 9B: 3D interaction model of Lig6 within the active site of mPGES-2, illustrating key hydrogen bonds and hydrophobic interactions. The ligand is shown in stick representation (cyan), while interacting residues are visualized with electrostatic surface rendering.

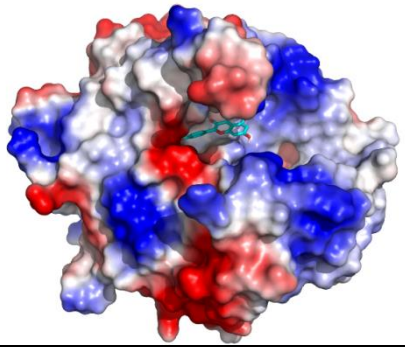

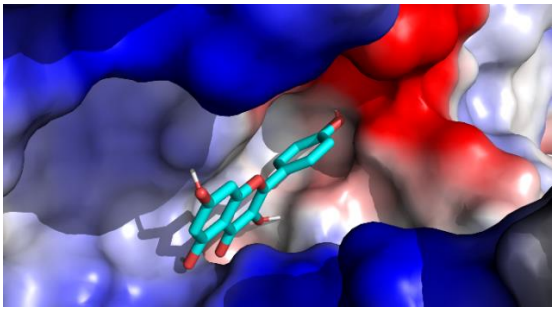

Figure 9C: 3D representation of mPGES-2 highlighting the electrostatic potential surface (blue: positive, red: negative) and the bound pose Lig6 (shown in cyan stick) embedded within the binding cavity.

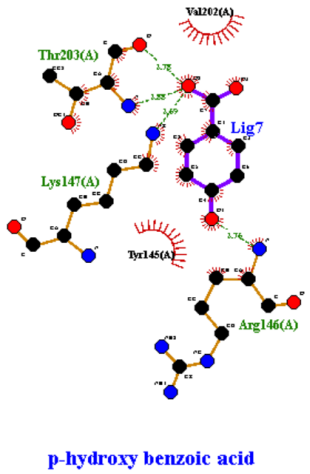

Figure 10A: 2D LigPlot+ interaction diagram of Lig7 showing hydrogen bonding (green dashed lines), and hydrophobic contacts (red arcs) with mPGES-2.

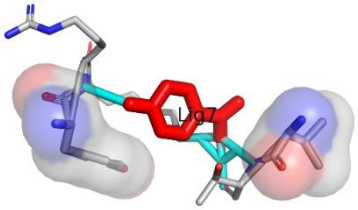

Figure 10B: 3D interaction model of Lig7 within the active site of mPGES-2, illustrating key hydrogen bonds and hydrophobic interactions. The ligand is shown in stick representation (cyan), while interacting residues are visualized with electrostatic surface rendering.

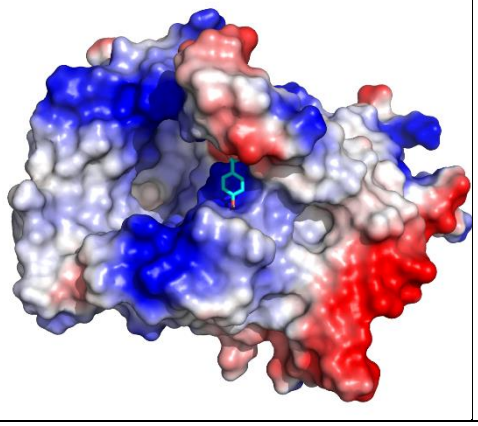

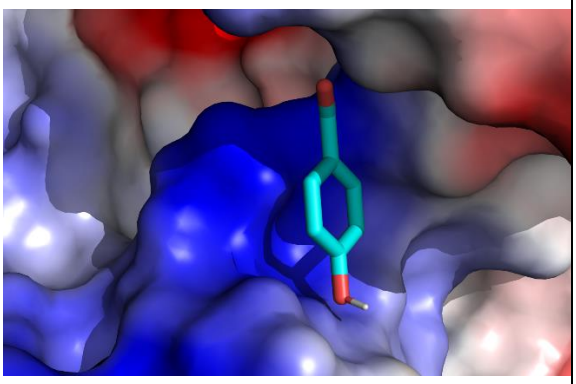

Figure 10C: 3D representation of mPGES-2 highlighting the electrostatic potential surface (blue: positive, red: negative) and the bound pose Lig7 (shown in cyan stick) embedded within the binding cavity.

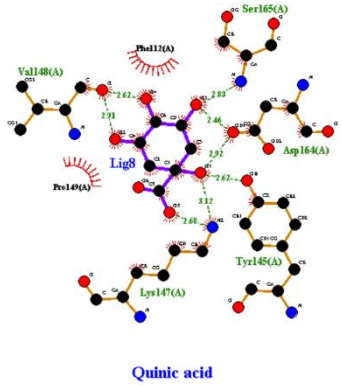

Figure 11: A2D LigPlot+ interaction diagram of Lig8 showing hydrogen bonding (green dashed lines), and hydrophobic contacts (red arcs) with mPGES-2.

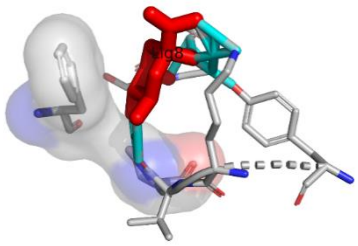

Figure 11B: 3D interaction model of Lig8 within the active site of mPGES-2, illustrating key hydrogen bonds and hydrophobic interactions. The ligand is shown in stick representation (cyan), while interacting residues are visualized with electrostatic surface rendering.

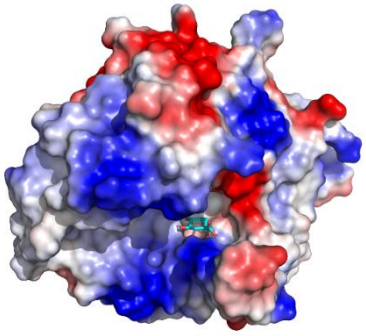

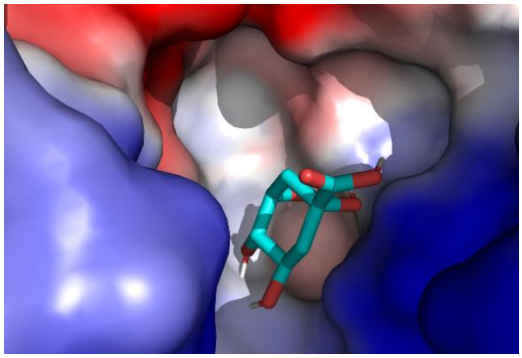

Figure 11C: 3D representation of mPGES-2 highlighting the electrostatic potential surface (blue: positive, red: negative) and the bound pose Lig8 (shown in cyan stick) embedded within the binding cavity.

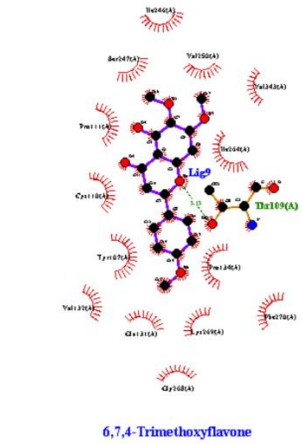

Figure 12 A: 2D LigPlot+ interaction diagram of Lig9 showing hydrogen bonding (green dashed lines), and hydrophobic contacts (red arcs) with mPGES-2.

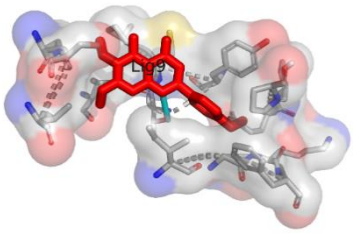

Figure 12B: 3D interaction model of Lig9 within the active site of mPGES-2, illustrating key hydrogen bonds and hydrophobic interactions. The ligand is shown in stick representation (cyan),

	while interacting residues are visualized with electrostatic surface rendering.
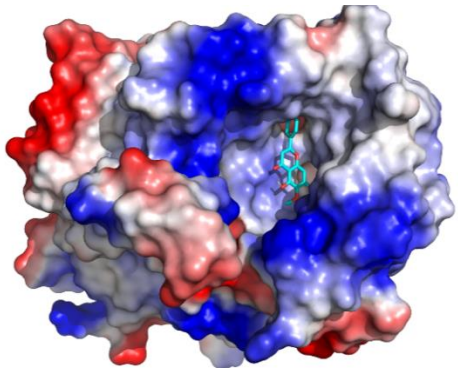	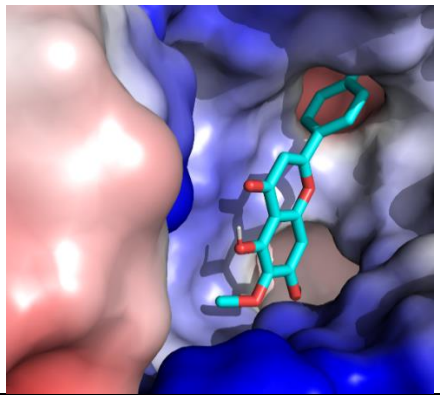

Figure 12C: 3D representation of mPGES-2 highlighting the electrostatic potential surface (blue: positive, red: negative) and the bound pose Lig9 (shown in cyan stick) embedded within the binding cavity.

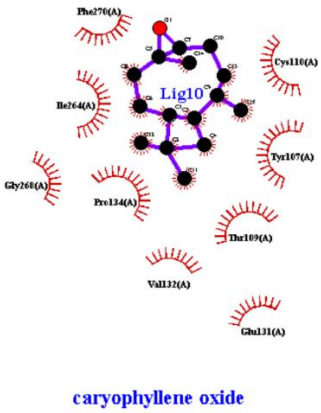	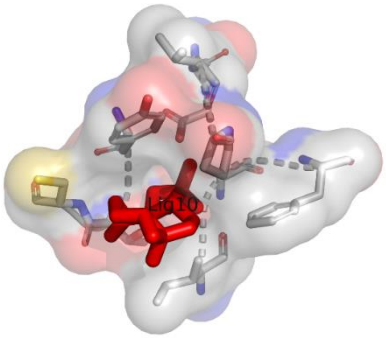
Figure 13A: 2D LigPlot+ interaction diagram of Lig10 showing hydrogen bonding (green dashed lines), and hydrophobic contacts (red arcs) with mPGES-2.	*Figure 13B: 3D interaction model of Lig10 within the active site of mPGES-2, illustrating key hydrogen bonds and hydrophobic interactions. The ligand is shown in stick representation (cya*
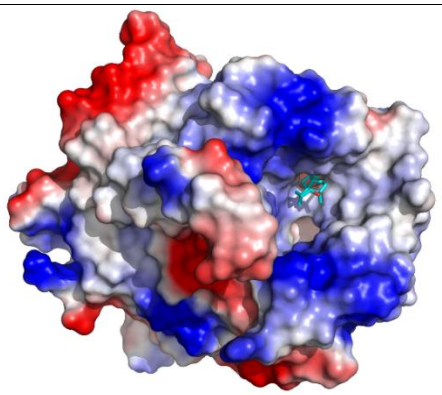	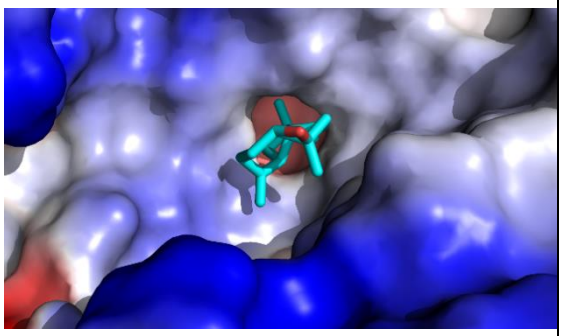

Figure 13C: 3D representation of mPGES-2 highlighting the electrostatic potential surface (blue: positive, red: negative) and the bound pose Lig10 (shown in cyan stick) embedded within the binding cavity.

Overall, the extract of *Vitex negundo* demonstrated potent anti-inflammatory and cytoprotective effects in vitro, with key phytoconstituents showing strong affinity and favorable pharmacokinetic profiles in silico.

Discussion

The in silico molecular docking study targeting prostaglandin E synthase-2 (mPGES-2) demonstrate a clear and dose-dependent inhibition of inflammation-associated biomarkers and enzyme activities, confirming the pharmacological relevance of *V. negundo* as a natural anti-inflammatory agent (Enechi et al., 2020). These are critical events mimicking inflammatory stress responses.

The pharmacological potential of *Vitex negundo* in inflammation management has been previously investigated in classical animal models. One of the oldest and pivotal study by Telang et al. (1999) demonstrated both peripheral and central analgesic activities of *V. negundo* leaf extract, along with anti-inflammatory effects in carrageenan-induced paw edema and granuloma pouch models in rats. Their findings attributed these actions primarily to the inhibition of prostaglandin synthesis, as evidenced by the extract's suppression of oxytocin-induced contractions in isolated uterine horns. However, the precise molecular targets and downstream immunomodulatory effects were not explored in that study (mPGES-2),

In a previous investigation by Dharmasiri et al., the aqueous extract of mature fresh leaves (MFL) of *V. negundo* was tested using classical in vivo rodent models of inflammation and nociception, including carrageenan-induced paw edema, formalin test, hot plate test, and tail flick assay. Their results highlighted potent oral anti-inflammatory, analgesic, antihistamine, membrane stabilizing, and antioxidant activities, along with an inverse dose-dependent inhibition of carrageenan-induced edema and formalin-induced chronic inflammation. Notably, they reported an EC_{50} of 2 g/kg for anti-inflammatory effects, and 4.1 g/kg for analgesic activity, without sedative or myorelaxant side effects (Dharmasiri et al., 2003).

Furthermore, Dharmasiri et al. proposed antihistamine and prostaglandin synthesis inhibition as major contributors to the pharmacological effects, based on indirect behavioral models and muscle coordination assessments.

A recent investigation such as that by Zhu et al. (2025), which undertook a comparative phytochemical and pharmacological analysis of different plant parts root (VNR), stem/leaf (VNSL), and fruit (VNF)—from *Vitex negundo L. var. cannabifolia*, a traditional Chinese variant which is widely used for rheumatic ailments in China. In Zhu et al.'s work, using UPLC-Q-TOF/MS, they identified a rich profile of flavonoids, lignans, terpenes, phenolic acids, and phenylpropanoids across all parts of the plant.

On the pharmacological front, Zhu et al. conducted in vivo animal experiments, including xylene-induced ear edema in mice, acetic acid-induced writhing, and CFA-induced arthritis models in rats. They observed that all three extracts significantly reduced edema and pain, with VNSL (stems and leaves) having the most pronounced anti-inflammatory activity, and VNF (fruits) showing the strongest analgesic response. While Zhu et al. did not directly assess the molecular targets or pathways involved, their cytokine analysis in arthritic rats notably decreased serum IL-1β, IL-6, and nitric oxide levels.

Our current study employed a structure-based drug design approach also, targeting prostaglandin E synthase-2 (mPGES-2) a critical enzyme downstream of COX-2 involved in inflammatory prostaglandin biosynthesis. Notably, ligands such as 2,3-dihydroxybenzoic acid and casticin exhibited strong binding energies and formed multiple hydrogen bonds and hydrophobic interactions with active site residues, suggesting potential inhibitory activity. These results not only corroborate the reduction in PGE_2 levels observed in vitro but also identify specific ligand-target interactions that can be further optimized for drug design.

Despite these encouraging findings, our study is not without limitations- invivo validation in rodent models of inflammation, followed by pharmacokinetic and toxicity profiling, will be essential for translational potential.

Overall, this study advances the pharmacological understanding of *Vitex negundo* by integrating in-vitro cytokine profiling with structure-based molecular docking. By targeting mPGES-2, a terminal enzyme in the prostaglandin synthesis cascade, this research elucidates a mechanistic pathway for its anti-inflammatory action. Unlike previous investigations limited to systemic animal models or general phytochemical screening, our approach offers both cellular-level validation and target-specific insight. These findings reinforce the therapeutic potential of *V. negundo* in chronic inflammatory disorders and

set the foundation for future translational and preclinical development.

Conclusion

This integrated in silico investigation establishes the anti-inflammatory potential of *Vitex negundo* phytoconstituents through molecular interaction studies. Collectively, the findings validate the traditional use of *Vitex negundo* in inflammatory conditions and highlight its promise as a multi-targeted phytotherapeutic agent. Further investigation, including compound isolation, mechanistic pathway analysis, and in vivo validation, is recommended to advance its development into a standardized anti-inflammatory formulation.

REFERENCES

1. Ciesielski, O., Biesiekierska, M., Panthu, B., Soszyński, M., Pirola, L., & Balcerczyk, A. (2022). Citrullination in the pathology of inflammatory and autoimmune disorders: recent advances and future perspectives. Cellular and Molecular Life Sciences, 79(2), 94.
2. Gusev, E., & Zhuravleva, Y. (2022). Inflammation: A new look at an old problem. International Journal of Molecular Sciences, 23(9), 4596.
3. Reichardt, S. D., Amouret, A., Muzzi, C., Vettorazzi, S., Tuckermann, J. P., Lühder, F., & Reichardt, H. M. (2021). The role of glucocorticoids in inflammatory diseases. Cells, 10(11), 2921.
4. Perveen, S., Khan, M. A., Parveen, R., Insaf, A., Parveen, B., Ahmad, S., & Husain, S. A. (2023). An updated review on traditional and modern aspects of vitex negundo. Current Traditional Medicine, 9(2), 114-127.
5. Dwivedi, M. K., Shukla, R., Sharma, N. K., Manhas, A., Srivastava, K., Kumar, N., & Singh, P. K. (2021). Evaluation of ethnopharmacologically selected Vitex negundo L. for In vitro antimalarial activity and secondary metabolite profiling. Journal of Ethnopharmacology, 275, 114076.
6. Heinrich, M., Jalil, B., Abdel-Tawab, M., Echeverria, J., Kulić, Ž., McGaw, L. J., ... & Wang, J. B. (2022). Best practice in the chemical characterisation of extracts used in pharmacological and toxicological research—the ConPhyMP—guidelines. Frontiers in Pharmacology, 13, 953205.
7. Nakka, H., Tiriveedhi, A., Ande, K., Kopuri, S., & Kandesi, H. (2025). Phytochemical Analysis and In-vitro Anti-inflammatory Activity of Proboscidea louisianica Leaf Extract Using HRBC Membrane Stabilization Assay. Journal of Pharma Insights and Research, 3(1), 173-177.
8. Lankatillake, C., Luo, S., Flavel, M., Lenon, G. B., Gill, H., Huynh, T., & Dias, D. A. (2021). Screening natural product extracts for potential enzyme inhibitors: protocols, and the standardisation of the usage of blanks in α-amylase, α-glucosidase and lipase assays. Plant Methods, 17(1), 3.
9. Esho, B. A., Samuel, B., Akinwunmi, K. F., & Oluyemi, W. M. (2021). Membrane stabilization and inhibition of protein denaturation as mechanisms of the anti-inflammatory activity of some plant species. Trends in Pharmaceutical Sciences and Technologies, 7(4), 269-278.
10. Arunachalam, K., & Sreeja, P. S. (2025). MTT Assay Protocol. In Advanced Cell and Molecular Techniques: Protocols for In Vitro and In Vivo Studies (pp. 271-276). New York, NY: Springer US.
11. Enechi, O. C., Okeke, E. S., Nwankwo, N. E., Nweze, J. E., Obilo, C. P., Okoye, C. I., & Awoh, O. E. (2020). Membrane stabilization, albumin denaturation, protease inhibition, and antioxidant activity as possible mechanisms for the anti-inflammatory effects of flavonoid-rich extract of Peltophorum pterocarpum (DC.) K. Heyne (FREPP) stem bark. Tropical Journal of Natural Product Research, 4(10), 812-816.
12. Telang, R. S., Chatterjee, S., & Varshneya, C. (1999). Studies on analgesic and anti-inflammatory activities of Vitex negundo Linn. Indian journal of pharmacology, 31(5), 363-366.
13. Dharmasiri, M. G., Jayakody, J. R. A. C., Galhena, G., Liyanage, S. S. P., & Ratnasooriya, W. D. (2003). Anti-inflammatory and analgesic activities of mature fresh leaves of Vitex negundo. Journal of ethnopharmacology, 87(2-3), 199-206.
14. Zhu, S., Shen, Y., & Zhang, Q. (2025). Comparison in chemical constituents and anti-inflammatory and analgesic effects of different medicinal parts from

a Vitex negundo L. var. cannabifolia. *Fitoterapia*, *185*, 106693. https://doi.org/10.1016/j.fitote.2025.106693